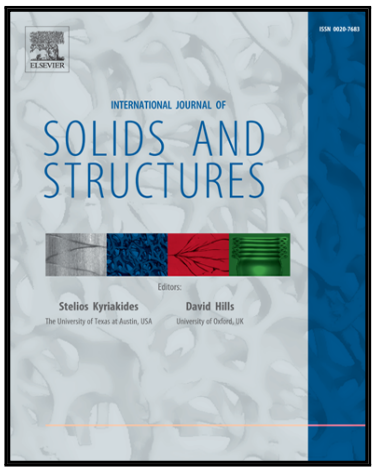

Stacked dielectric tubes with electromechanically controlled radii

Noy Cohen

PII: S0020-7683(16)30262-1
DOI: 10.1016/j.ijsolstr.2016.09.014
Reference: SAS 9300

To appear in: *International Journal of Solids and Structures*

Received date: 5 June 2016
Revised date: 6 September 2016
Accepted date: 12 September 2016

Please cite this article as: Noy Cohen, Stacked dielectric tubes with electromechanically controlled radii, *International Journal of Solids and Structures* (2016), doi: 10.1016/j.ijsolstr.2016.09.014

Stacked dielectric tubes with electromechanically controlled radii

Noy Cohen[1,2] *

[1]Dept. of Mechanical Engineering, Ben-Gurion University, Beer-Sheva 84105, Israel

[2]Division of Engineering and Applied Science, California Institute of Technology, Pasadena, CA 91125, USA

Abstract

This work examines the features and capabilities of a tube comprised of stacked cylindrical dielectric layers separated by flexible electrodes with the applicative aim of electrically controlling the inner radius. The study begins with the analysis of the non-homogenous electromechanical response of a single-layer dielectric tube according to well-established coupled models. Two boundary conditions are examined - traction free boundaries and a fixed outer radius. The advantages and limitations of each boundary conditions are discussed. It is shown that dielectric tubes subjected to traction free boundaries experience instabilities, an effect that can be avoided by fixing the outer surface. Next, the electromechanical behavior of a stacked cylindrical actuator comprised of dielectric tubes that are mechanically connected in series and electrically connected in parallel is determined under the two boundary conditions discussed above. It is shown that the stacking of cylindrical layers increases the range of available inner radii at the cost of design limitations. Interestingly, it is found that mounting layers on a stacked cylindrical actuator may lead to instabilities even if the outer radius is fixed.

Keywords: electro-active polymers, smart materials, stacked dielectrics

1 Introduction

Electro-active polymers (EAPs) are materials that deform as a result of electric excitation. These elastomers possess many promising properties such as low density, flexibility, ability to undergo large deformations, fast response and availability. Therefore, EAPs are employed in many actuation-based applications such as artificial muscles (Bar-Cohen, 2001), energy-harvesting

*Corresponding Author. E-mail: noyco5@gmail.com

devices (Springhetti et al., 2014; McKay et al., 2010), micropumps (Rudykh et al., 2012) and tunable wave guides (Shmuel and deBotton, 2013), among others. The actuation is the result of the attraction between two oppositely charged electrodes that are attached to a thin dielectric film. Due to the Poisson's effect, the film compresses in thickness and expands in the transverse direction.

Depending on the application, EAPs may be employed in various configurations such as flat films, dielectric tubes and dielectric spheres. For example, energy harvesting devices are comprised of elastomer sheets that are used to transform mechanical energy into electrical energy (Due et al., 2010; McKay et al., 2010; Tutcuoglu and Majidi, 2014). Another novel application that is based on EAP films is the stacked dielectric elastomer actuator. This device is comprised of stacked capacitors, where each capacitor is composed of two thin flexible conductive layers that are perfectly adhered to an incompressible EAP film. The capacitors are mechanically connected in series and electrically connected in parallel. An electric field is applied across the thickness of the films and compresses them. Typically, these devices are composed of a large number of films to obtain a large cumulative displacement. Three types of stacking have been proposed: multi-layer stacking (Schlaak et al., 2005; Kovacs and Düring, 2009; Kovacs et al., 2009; Lotz et al., 2011), where separate EAP films are stacked on top of each other, stacking in a helical structure (Carpi et al., 2005), and a folded dielectric elastomer (Carpi et al., 2007), where an EAP strip is coated with flexible electrodes and folded to a stacked shape. Practically, Kovacs et al. (2009) demonstrated that such a device composed of ~ 350 dielectric films is capable of lifting a weight of $2.1\,[\mathrm{kg}]$ to a height $2.5\,[\mathrm{mm}]$. The capabilities of this actuator were theoretically examined by Moscardo et al. (2008) and Cohen (2016), among others.

Pei et al. (2003) proposed to use EAPs as cylindrical actuators, or tubes, in a spring roll configuration. This actuator is comprised of EAP films that are stacked and wrapped around an elastic coil spring. An electric field is then applied across the layers and compresses them. This, in turn, induces an axial extension of the device. Kovacs et al. (2007) employed this motion in an arm wrestling robot. Another actuation that is based on a cylindrical configuration was proposed by Shmuel and deBotton (2013) and Shmuel (2015). These works studied the propagation of longitudinal and torsional waves in dielectric elastomer tubes. From a theoretical point of view, Carpi and De Rossi (2004) and Singh and Pipkin (1966) examined the electromechanical response of tubes under small and finite deformations, respectively.

This work examines the capabilities of soft tubes with electromechanically controlled radii. Consider an actuator that is comprised of stacked cylindrical capacitors, where each capacitor is made of two flexible cylindrical conductive layers that are perfectly adhered to a thin-wall dielectric tube. The tubes are mechanically connected in series and electrically connected in parallel. The capacitors are mounted on a soft dielectric vessel that holds the structure together. The conductive layers are charged with alternating polarities such that the same voltage is ap-

plied across each dielectric tube. Note that due to the geometry of the device, the induced electric field, and consequently the resulting deformation, are non-homogenous. The electric forces compress the layers and as a consequence, the inner radius increases and the inner tube expands. This allows to control the opening of the soft dielectric vessel by an applied voltage. This device may be used in many applications such as, for example, increasing or decreasing the pressure, the velocity or the rate of flow of fluid through a pipe.

This work begins with a short theoretical background. The electro-mechanical response of a single-layer tube is studied according to two electromechanical models under two boundary conditions with the practical aim of finding the design that maximizes the range of available inner radii of the tube. Next, the behavior of a stacked cylindrical actuator is examined. The effects of the boundary conditions and the influence of the number of dielectric layers is discussed. The conclusions are gathered in the last section.

2 Theoretical background

Consider the deformation of a hyper-elastic dielectric subjected to an electro-mechanical loading. The continuum occupies a region $\Omega_0 \subset \mathbb{R}^3$ with a boundary $\partial\Omega_0$ before the deformation and a region $\Omega \subset \mathbb{R}^3$ with a boundary $\partial\Omega$ at the current configuration. The material points at the reference and the current configurations are denoted by $\mathbf{X}$ and $\mathbf{x}$, respectively. The mapping of the material points is $\mathbf{x} = \boldsymbol{\varphi}(\mathbf{X})$ and the corresponding deformation gradient is

$$\mathbf{F} = \nabla_{\mathbf{X}} \boldsymbol{\varphi}(\mathbf{X}), \tag{1}$$

where $\nabla_{\mathbf{X}}$ is the gradient operation with respect to the referential coordinate system. The right and left Cauchy-Green strain tensors are defined as $\mathbf{C} = \mathbf{F}^T \mathbf{F}$ and $\mathbf{b} = \mathbf{F}\mathbf{F}^T$, respectively. The ratio between infinitesimal volume elements in the current and the reference configurations is $J = \det \mathbf{F} > 0$. Within the current framework, only incompressible materials are considered and therefore $J = 1$.

The dielectric is subjected to an electric field

$$\mathbf{E}(\mathbf{x}) = -\nabla_{\mathbf{x}} \phi, \tag{2}$$

where $\phi(\mathbf{x})$ is the scalar electric potential and $\nabla_{\mathbf{x}}$ is carried out with respect to the current coordinate system. The electric field satisfies Faraday's law, $\nabla_{\mathbf{x}} \times \mathbf{E} = \mathbf{0}$, throughout the entire space. The electric displacement field is

$$\mathbf{D}(\mathbf{x}) = \varepsilon_0 \mathbf{E}(\mathbf{x}) + \mathbf{P}(\mathbf{x}), \tag{3}$$

where ε_0 is the permittivity of vacuum and $\mathbf{P}(\mathbf{x})$ is the polarization, or the electric dipole-density. Recall that in vacuum $\mathbf{P} = \mathbf{0}$. In ideal dielectrics there are no free charges and therefore the electric displacement inside the dielectric is governed by the equation

$$\nabla_{\mathbf{x}} \cdot \mathbf{D} = 0. \tag{4}$$

This relation also holds in the vacuum surrounding the dielectric.

The referential counterparts $\mathbf{E}^{(0)}$ and $\mathbf{D}^{(0)}$ of the electric field and the electric displacement are (Dorfmann and Ogden, 2005)

$$\mathbf{E}^{(0)} = \mathbf{F}^T \mathbf{E}, \tag{5}$$

and

$$\mathbf{D}^{(0)} = \mathbf{F}^{-1} \mathbf{D}. \tag{6}$$

With the above definitions, $\nabla_{\mathbf{X}} \times \mathbf{E}^{(0)} = \mathbf{0}$ and $\nabla_{\mathbf{X}} \cdot \mathbf{D}^{(0)} = 0$ inside the dielectric and in the surrounding vacuum. Since the referential polarization $\mathbf{P}^{(0)}$ is not uniquely defined, I follow Dorfmann and Ogden (2005) and Cohen et al. (2016) and adopt the definition

$$\mathbf{P}^{(0)} = \mathbf{F}^{-1} \mathbf{P}, \tag{7}$$

Note that with this definition, the referential polarization and the referential electric field are energy conjugates such that $\frac{1}{J} \mathbf{E}^{(0)} \cdot \mathbf{P}^{(0)} = \mathbf{E} \cdot \mathbf{P}$.

The stress and the polarization that develop in hyper-elastic dielectrics can be derived from a scalar energy-density function $\Psi\left(\mathbf{F}, \mathbf{E}^{(0)}\right)$. This work assumes that the energy-density function can be decomposed into a mechanical and a coupled contributions (Dorfmann and Ogden, 2005; McMeeking et al., 2007; Cohen and deBotton, 2014; Cohen et al., 2016),

$$\Psi\left(\mathbf{F}, \mathbf{E}^{(0)}\right) = \Psi_m\left(\mathbf{F}\right) + \Psi_c\left(\mathbf{F}, \mathbf{E}^{(0)}\right), \tag{8}$$

where $\Psi_m(\mathbf{F})$ characterizes the response of the material in the absence of electrical forces and $\Psi_c\left(\mathbf{F}, \mathbf{E}^{(0)}\right)$ accounts for the difference between Ψ with and without electric excitation. Accordingly, the electric displacement is determined via

$$\mathbf{D} = -\mathbf{F} \frac{\partial \Psi_c\left(\mathbf{F}, \mathbf{E}^{(0)}\right)}{\partial \mathbf{E}^{(0)}}, \tag{9}$$

and the stress that develops in the material is

$$\begin{aligned}\boldsymbol{\sigma} &= \frac{\partial \Psi\left(\mathbf{F}, \mathbf{E}^{(0)}\right)}{\partial \mathbf{F}} \mathbf{F}^T - p\,\mathbf{I} \\ &= \left(\frac{\partial \Psi_m\left(\mathbf{F}\right)}{\partial \mathbf{F}} + \frac{\partial \Psi_c\left(\mathbf{F}, \mathbf{E}^{(0)}\right)}{\partial \mathbf{F}} \right) \mathbf{F}^T - p\,\mathbf{I}.\end{aligned} \tag{10}$$

The last term in Eq. (10) is a workless pressure-like term stemming from the incompressibility of the the dielectric. It is determined from the equilibrium equations and the boundary conditions.

The electrical boundary conditions are given in terms of either the electric potential or the charge per unit area ρ_s, such that

$$[\![\mathbf{E}]\!] \times \hat{\mathbf{n}} = \mathbf{0}; \qquad [\![\mathbf{D}]\!] \cdot \hat{\mathbf{n}} = -\rho_s, \tag{11}$$

where $[\![\bullet]\!] = \bullet^{(i)} - \bullet^{(o)}$ denotes the jump in the vectorial quantity $\bullet$ across the boundary, $\bullet^{(i)}$ and $\bullet^{(o)}$ are the vectors inside and outside the dielectric, respectively, and $\hat{\mathbf{n}}$ is the outward pointing unit normal to the boundary at the current configuration. Practically, in common EAPs settings ρ_s is the charge on the electrodes. The mechanical boundary conditions are given in terms of the displacement of the boundary or the mechanical traction $\mathbf{t}$ such that

$$[\![\boldsymbol{\sigma}]\!]\, \hat{\mathbf{n}} = \mathbf{t}. \tag{12}$$

Outside the body, the electric field induces the the Maxwell stress

$$\boldsymbol{\sigma}^v = \varepsilon_0 \left(\mathbf{E} \otimes \mathbf{E} - \frac{1}{2} \left(\mathbf{E} \cdot \mathbf{E} \right) \mathbf{I} \right). \tag{13}$$

The stress satisfies the equilibrium equation

$$\nabla_{\mathbf{x}} \cdot \boldsymbol{\sigma} = \mathbf{0}, \tag{14}$$

throughout the entire space, where the body forces are neglected.

2.1 Coupled constitutive relations

Following the work of Dorfmann and Ogden (2005), this work employs the coupled energy-density function

$$\Psi_c\left(\mathbf{F}, \mathbf{E}^{(0)}\right) = -\frac{\varepsilon_r \varepsilon_0}{2} \mathbf{E}^{(0)} \cdot \mathbf{C}^{-1} \mathbf{E}^{(0)}, \tag{15}$$

where ε_r is the relative permittivity. Accordingly, Eq. (9) is employed to obtain the electric displacement

$$\mathbf{D} = \varepsilon_r \varepsilon_0 \mathbf{E}, \tag{16}$$

where Eq. (5) is used. For later reference, also note that

$$\frac{\partial \Psi_c \left(\mathbf{F}, \mathbf{E}^{(0)}\right)}{\partial \mathbf{F}} = \varepsilon_r \varepsilon_0 \left(\mathbf{E} \otimes \mathbf{E}\right) \mathbf{F}^{-T}. \tag{17}$$

Numerous energy-density functions have been proposed to characterize the mechanical behavior of the dielectric. The simplest one is the well-known neo-Hookean model,

$$\Psi_m^{nH} \left(\mathbf{F}\right) = \frac{\mu}{2} \left(I_1 - 3\right), \tag{18}$$

where μ is the shear modulus and $I_1 = \mathrm{tr}\left(\mathbf{C}\right)$ is the first invariant of the right Cauchy-Green strain tensor. Here, $\mathrm{tr}\left(\mathbf{C}\right)$ denotes the trace of $\mathbf{C}$. Note that this model contains only one material parameter. The coupled resulting stress is computed with Eq. (10),

$$\boldsymbol{\sigma}^{nH} = \mu \mathbf{b} + \varepsilon_r \varepsilon_0 \mathbf{E} \otimes \mathbf{E} - p\mathbf{I}, \tag{19}$$

where Eq. (17) is employed.

The Gent model is also frequently used to characterize the mechanical behavior of elastomers (Gent, 1996). This phenomenological model accounts for the lock-up effect seen in elastomers. The Gent energy-density function is

$$\Psi_m^{G} \left(\mathbf{F}\right) = -\frac{\mu J_m}{2} \ln\left(1 - \frac{I_1 - 3}{J_m}\right), \tag{20}$$

where $J_m = I_1^{lu} - 3$ is a material parameter determined from the value of the first invariant at the lock-up stretch I_1^{lu}. Note that as $I_1 \to J_m + 3$, $\Psi_m^{G} \left(\mathbf{F}\right) \to \infty$ thus capturing the lock up effect. The stress according to the Gent model is determined with Eqs. (10) and (17),

$$\boldsymbol{\sigma}^{G} = \frac{\mu J_m}{J_m - I_1 + 3} \mathbf{b} + \varepsilon_r \varepsilon_0 \mathbf{E} \otimes \mathbf{E} - p\mathbf{I}. \tag{21}$$

In the following, we employ the two discussed constitutive models and examine the electro-mechanical response of soft dielectric tubes.

3 The electro-mechanical response of a single layer tube

The electro-mechanical behavior of dielectric elastomer tubes has been previously modeled for small and finite deformations by Carpi and De Rossi (2004) and Singh and Pipkin (1966), re-

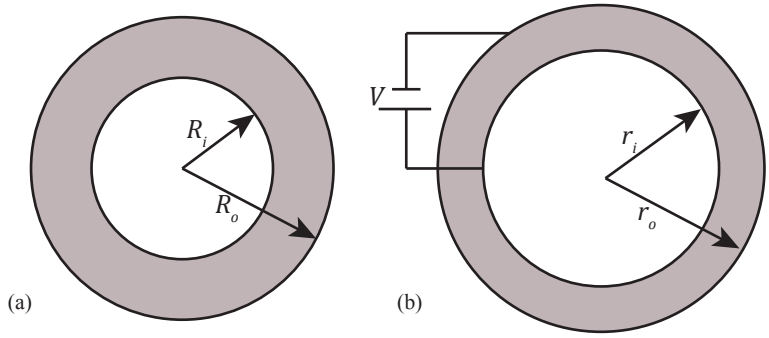

Figure 1: A cross section of a single layer tube (a) before and (b) after actuation.

spectively. Following these works, the applicative aim of this paper is to examine the expansion of the inner tube under an applied voltage and to demonstrate that the inner radius can be electrically controlled. To this end, the solution proposed by Singh and Pipkin (1966) is employed and two boundary conditions are examined.

Consider the deformation of an infinite incompressible soft dielectric tube with initial inner and outer radii R_i and R_o, respectively (Fig. (1a)). The inner and outer surfaces are coated with flexible electrodes. The referential material points are described in a cylindrical coordinate system (R, Θ, Z) where $R_i \leq R \leq R_o$ and $0 \leq \Theta \leq 2\pi$. A voltage V is applied across the thickness of the tube and induces a radial electric field which, in turn, deforms the tube. At the current configuration the inner and outer radii are denoted r_i and r_o, respectively (Fig. (1b)). The mapping of the material points is

$$r = \sqrt{A\,R^2 + B}; \qquad \theta = \Theta; \qquad z = \frac{Z}{A}, \tag{22}$$

where $r_i \leq r \leq r_o$, $0 \leq \theta \leq 2\pi$ and the constants A and B characterize the deformation and are determined from the boundary conditions. Consequently, the deformation gradient is

$$\mathbf{F} = \begin{pmatrix} \frac{\partial r}{\partial R} & 0 & 0 \\ 0 & \frac{r}{R}\frac{\partial \theta}{\partial \Theta} & 0 \\ 0 & 0 & \frac{\partial z}{\partial Z} \end{pmatrix} = \begin{pmatrix} \frac{A\,R}{\sqrt{A\,R^2+B}} & 0 & 0 \\ 0 & \frac{\sqrt{A\,R^2+B}}{R} & 0 \\ 0 & 0 & \frac{1}{A} \end{pmatrix}. \tag{23}$$

Note that this deformation gradient satisfies the incompressibility constraint $J = 1$.

The radial electric field induced by the potential difference V inside the dielectric is

$$\mathbf{E} = \frac{V}{\ln\left(\frac{r_o}{r_i}\right)} \frac{1}{r}\,\hat{\mathbf{r}}, \tag{24}$$

and in the vacuum surrounding the tube $\mathbf{E} = \mathbf{0}$. The resulting stress according to the neo-Hookean and the Gent based models is obtained via Eqs. (19) and (21), respectively.

The equilibrium equations along the θ and the z directions are automatically satisfied with the considered models. The pressure term $p = p(r)$ is determined from the equilibrium along the r direction,

$$\frac{\partial \sigma_{rr}}{\partial r} + \frac{\sigma_{rr} - \sigma_{\theta\theta}}{r} = 0. \tag{25}$$

Additionally, the tube is free to expand along the axial direction and therefore,

$$\int_{r_i}^{r_o} \int_{0}^{2\pi} \sigma_{zz}\, r \, \mathrm{d}r \, \mathrm{d}\theta = 0. \tag{26}$$

According to the neo-Hookean model, the resulting pressure term is

$$p(r) = \frac{A\,\mu}{2}\left(\ln\left(\eta^{nH}\right) - \frac{B}{r^2}\right) + \frac{\varepsilon_r \varepsilon_0}{2}\left(\frac{V}{\ln\left(\frac{r_o}{r_i}\right)}\right)^2 \frac{1}{r^2} + C, \tag{27}$$

where Eqs. (19) and (25) are employed and $\eta^{nH} = \frac{r^2}{r^2 - \gamma}$. The integration constant

$$C = \frac{\mu}{A^2} + \frac{1}{r_o^2 - r_i^2}\left(\frac{A\,\mu}{2}\left(r_i^2 \ln\left(\eta_i^{nH}\right) - r_o^2 \ln\left(\eta_o^{nH}\right) + B\,\ln\left(\frac{\eta_o^{nH}}{\eta_i^{nH}}\right)\right) - \varepsilon_r \varepsilon_0 \frac{V^2}{\ln\left(\frac{r_o}{r_i}\right)}\right), \tag{28}$$

is determined from Eq. (26), where η_i^{nH} and η_o^{nH} take the value of η^{nH} with $r = r_i$ and $r = r_o$, respectively.

Substituting the stress according to the mechanical Gent model (Eq. (21)) into Eq. (25) results in the pressure term,

$$p = \frac{J_m \mu}{4\eta_1}\left(\frac{4A^3 B}{\eta_3}\left(\eta_1^2\left(r^2 - B\right) - A^3 B\right) + \eta_1^2 \ln\left(\frac{\eta 3}{r^4}\right) - \eta_1 \eta_2 \ln(f)\right) + \frac{\varepsilon_r \varepsilon_0}{2}\left(\frac{V}{\ln\left(\frac{r_o}{r_i}\right)}\right)^2 \frac{1}{r^2} + C, \tag{29}$$

where $\eta_1 = \sqrt{A^2(3 + J_m) - 1 - 2A^3}$, $\eta_2 = \sqrt{A^2(3 + J_m) - 1 + 2A^3}$, $\eta_3 = A^3 B^2 + \eta_1^2 r^2 (B - r^2)$ and

$$f = \frac{B(\eta_2 + \eta_1) - 2r^2 \eta_1}{B(\eta_2 - \eta_1) + 2r^2 \eta_1}. \tag{30}$$

Practically, $J_m \gg A$ and therefore the expressions in the square root of η_1 is greater than zero. It is also noted that within the range of practical values discussed hereafter, $\eta_2 > 0$, $\eta_3 > 0$ and

$f > 0$. The integration constant C is determined from Eq. (26)

$$C = \frac{J_m \mu}{\eta_1^2} + \frac{1}{r_o^2 - r_i^2}\left(r_i^2\left(\ln\left(\frac{\eta_{3i}}{r_i^4}\right) - \frac{\eta_2}{\eta_1}\ln\left(f_i\right)\right) - r_o^2\left(\ln\left(\frac{\eta_{3o}}{r_o^4}\right) - \frac{\eta_2}{\eta_1}\ln\left(f_o\right)\right) + \frac{2\,A^3 B}{\eta_1^3 \eta_2}\left(3 - A^2\left(3 + J_m\right)\right)\ln\left(\frac{f_o}{f_i}\right)\right), \tag{31}$$

where f_i and η_{3i} assume the values of f and η_3 with $r = r_i$ and f_o and η_{3o} take the values of f and η_3 with $r = r_o$.

In the following, three tubes made of EAPs with different wall thicknesses are examined. The properties of the EAPs are those of the VHB 4910 dielectric. Specifically, the shear modulus and the permittivity are $\mu = 73\,[\mathrm{kPa}]$ and $\varepsilon_r = 4.7$, respectively, and the Gent material parameter $J_m = 89$ is determined from a uniaxial extension experiment where the measured lock-up stretch was 9.6 (Bozlar et al., 2012). The inner referential radius of the three tubes is $R_i = 1\,[\mathrm{mm}]$ and the outer referential radii are $R_o = 1.1\,[\mathrm{mm}]$, $R_o = 1.4\,[\mathrm{mm}]$ and $R_o = 2\,[\mathrm{mm}]$. The ratio between the wall thickness $H = R_o - R_i$ and the average referential radius $\langle R\rangle = \frac{R_o + R_i}{2}$ of the three tubes is $\frac{H}{\langle R\rangle} = 0.095, \frac{1}{3}, \frac{2}{3}$. Throughout this section, these tubes are referred to as the thin, the intermediate and the thick wall tubes, respectively.

The constants A and B are determined from the boundary conditions on the inner and outer surfaces of the tube. First, two types of boundary conditions are examined with the aim of maximizing the range of available inner radii:

1. *Traction free tube* - the inner and outer surfaces of the tube are free to deform under the influence of an electric field,

$$\sigma_{rr}\left(r_i\right) = 0; \qquad \sigma_{rr}\left(r_o\right) = 0. \tag{32}$$

2. *Fixed outer radius* - the outer surface of the tube is fixed while the internal surface is traction free,

$$r_o = R_o; \qquad \sigma_{rr}\left(r_i\right) = 0. \tag{33}$$

For convenience, I define the dimensionless quantities $\overline{V} = \frac{V}{H}\sqrt{\frac{\varepsilon_r \varepsilon_0}{\mu}}$, $\overline{h} = \frac{r_o - r_i}{H}$, $\overline{r_i} = \frac{r_i}{R_i}$ and $\overline{r_o} = \frac{r_o}{R_o}$ which correspond to the normalized applied voltage, the relative wall thickness, and the relative inner and outer radii, respectively.

Figs. (2a) and (2d) depict the relative inner radius $\overline{r_i}$ and the relative wall thickness $\overline{h}$ as a function of the normalized voltage $\overline{V}$ for the thin tube under traction free boundary conditions (Eq. (32)). Throughout this work, the continuous and the dashed curves correspond to the predictions according to the neo-Hookean and to the Gent models, respectively. Note that at a critical voltage $\overline{V}_c \approx 0.7$ the tube experiences an instability. According to the mechanical neo-Hookean model, no physical solutions exist for voltages $\overline{V} > 0.7$. This is expected since

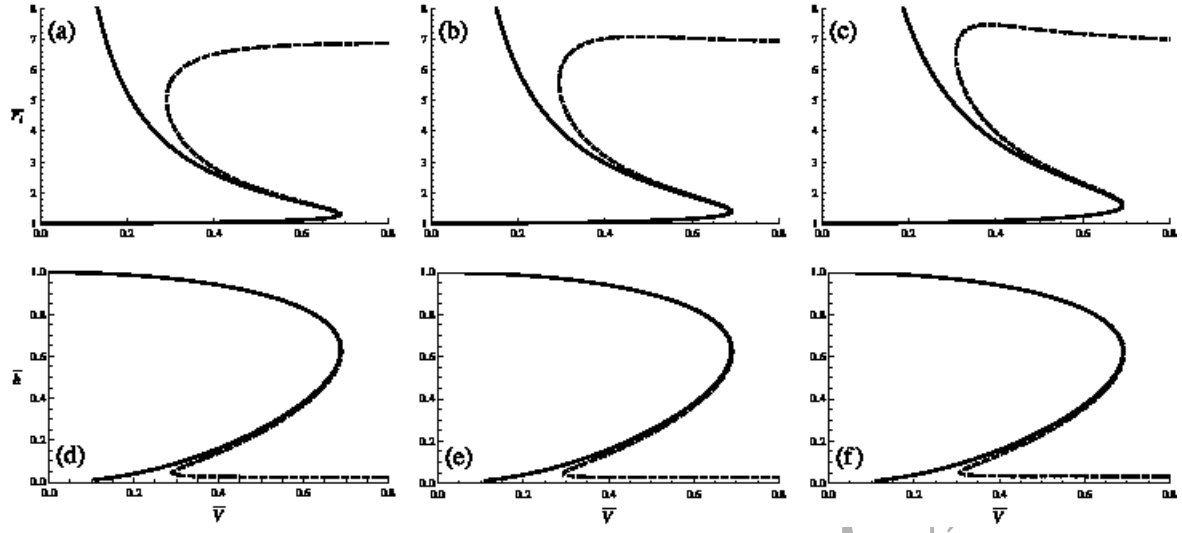

Figure 2: The relative inner radius $\overline{r_i}$ (a-c) and the relative wall thickness $\overline{h}$ (d-f) as a function of the normalized applied voltage $\overline{V}$ under traction free boundary conditions. The continuous and the dashed curves correspond to the predictions of the neo-Hookean (Eq. (19)) and the Gent (Eq. (21)) models, respectively. Figs. (a,d), (b,e) and (c,f) correspond to the thin, the intermediate and the thick wall tubes, respectively.

the neo-Hookean behavior does not account for the lock-up effect. The mechanical Gent model predicts that at this critical voltage the tube experiences a rapid reduction in thickness, as shown in Fig. (2d), and a sharp expansion of the inner radius of the tube, as shown in Fig. (2a). This phenomenon is known as the snap-through effect and is widely discussed in several works (Suo et al. 2008; Rudykh et al. 2012; Cohen et al. 2016). To explain this behavior, note that the electrical stress intensifies as a result of two factors - the increase in the voltage and the reduction in the wall thickness of the tube. Beyond a critical normalized voltage $\overline{V}_c$, the neo-Hookean model predicts that the increase in the electrical stress cannot be compensated by a mechanical stress and equilibrium cannot be reached. According to the Gent model, in order to achieve traction free boundaries with a normalized voltage $\overline{V} > \overline{V}_c$, the tube wall must significantly thin to a point that is near the lock up stretch. Such a deformation gives rise to a high mechanical stress that satisfies equilibrium. It is emphasized that throughout the snap-through process, the inner and the outer radii of the tube increase. However, since the intensity of the electric field decays with the ratio $\frac{1}{r}$ (Eq. (24)), the electrical forces on the outer boundary are weaker than those on the inner boundary and the tube wall significantly thins as well. Note that the loading and unloading paths of the voltage according to the Gent model differ. Specifically, decreasing the voltage to $\overline{V} \approx 0.3$ after the instability occurred results in a sharp expansion of the tube wall and a reduction in $\overline{r_i}$.

Figs. (2b) and (2c) depict the relative inner radius $\overline{r_i}$ as a function of the normalized voltage $\overline{V}$ for the intermediate and the thick wall tubes, respectively. It is shown that the normalized

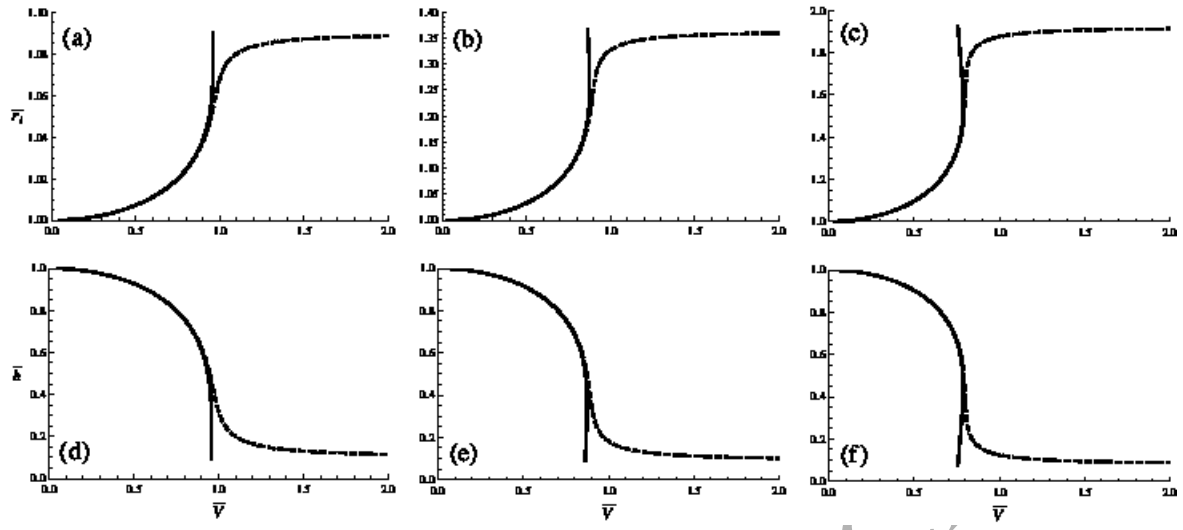

Figure 3: The relative inner radius $\overline{r_i}$ (a-c) and the relative wall thickness $\overline{h}$ (d-f) as a function of the normalized applied voltage $\overline{V}$ under a fixed outer radius. The continuous and the dashed curves correspond to the neo-Hookean (Eq. (19)) and the Gent (Eq. (21)) models, respectively. Figs. (a,d), (b,e) and (c,f) correspond to the thin, the intermediate and the thick tubes, respectively.

critical voltage at which instability occurs is similar for the three discussed tubes. However, since $\overline{V}$ is normalized by H the applied voltage V required to achieve $\overline{V}_c$ is higher in thicker wall tubes. Furthermore, the three tubes have the same initial inner radius and therefore we find that an inner radius r_i can be achieved with lower voltages at thinner wall tubes. This is expected since the magnitude of the electric field in thinner tubes is higher. For example, a relative inner radius $\overline{r_i} = 1.1$ is obtained with $V \approx 2.4\,[\mathrm{kV}]$, $V \approx 8.7\,[\mathrm{kV}]$ and $V \approx 18\,[\mathrm{kV}]$ in a thin, an intermediate and a thick wall tube subjected to traction free boundaries, respectively. Therefore, thin wall tubes are preferable for the discussed envisaged application.

Figs. (2e) and (2f) depict the relative wall thickness $\overline{h}$ as a function of the normalized voltage $\overline{V}$ for the intermediate and the thick tubes, respectively. A comparison with Fig. (2d) for the thin tube reveals that the dependence of the relative wall thickness $\overline{h}$ on the applied voltage is similar for the three considered tubes. However, recall that $\overline{h}$ is proportional to one over the initial wall thickness and therefore the wall thickness of the thick tube in a deformed configuration is greater than that of the thin tube. This effect should be taken into consideration in the design of soft tubes with the purpose of an electrically controlled inner radius.

To conclude, for the purpose of the envisaged application we find that under traction free boundary conditions the thin tube is superior - a similar range of inner radii can be achieved with lower voltages.

Next we examine the response of the three tubes subjected to an applied voltage under a fixed outer radius (Eq. (33)). Figs. (3a) and (3d) plot the relative inner radius $\overline{r_i}$ and the relative wall thickness $\overline{h}$ as a function of the normalized voltage $\overline{V}$ for the thin tube. Since the outer

radius is fixed, the displacement of the inner radius is limited and consequently a smaller range of inner radii is available in comparison with the traction free tube. In addition, we find that according to the neo-Hookean behavior no physical solutions exist beyond a voltage $\overline{V} \approx 0.92$. However, the Gent model suggests that any voltage can be applied and predicts a lock up at a wall thickness $\overline{h} \approx 0.1$. Due to the fixed outer radius, at high voltages the wall thickness is larger than that of a tube subjected to traction free boundaries. Consequently, it is pointed out that a compressive stress is required in order to hold the outer surface fixed. Interestingly, the Gent model does not predict instabilities under these boundary conditions.

Following the applicative interest of this paper, note that significantly lower voltages are required to attain a given displacement of the inner radius in tubes subjected to traction free boundary conditions. Specifically, a relative inner radius $\overline{r_i} = 1.05$ is achieved with $V \approx 1.9\,[\mathrm{kV}]$ (Fig. (2a)) and $V \approx 3.9\,[\mathrm{kV}]$ (Fig. (3a)) in a thin wall tube subjected to traction free and fixed outer radius boundary conditions, respectively. Therefore, traction free boundaries are preferable for this application.

Figs. (3b) and (3e) plot the relative inner radius $\overline{r_i}$ and the relative thickness $\overline{h}$ as a function of the normalized voltage $\overline{V}$ for the intermediate tube. A comparison with the predictions under traction free boundary conditions (Figs. (2b) and (2e)) reveals that, as stated with regard to the thin wall tube, fixing the outer radius increases the voltages required for radial expansions. It is also pointed out that the range of available inner radii in intermediate tubes is greater than that of thin tubes (note the scales of $\overline{r_i}$ in figs. (3a) and (3b)). However, as previously mentioned, the shortcoming of tubes with thicker walls is that the same radial expansions are achieved with higher voltages.

The relative inner radius $\overline{r_i}$ and the relative thickness $\overline{h}$ as a function of the normalized voltage $\overline{V}$ for the thick wall tube are illustrated in Figs. (3c) and (3f). The thick wall of the tube allows for a higher range of inner radii at the cost of higher applied voltages. Interestingly, the dependence of the relative wall thickness $\overline{h}$ on the applied voltage $\overline{V}$ is similar for the three considered tubes, as can be seen from Figs. (3d), (3e) and (3f). Furthermore, it is concluded that a compressive stress is required in order to keep the outer radius fixed in the three discussed tubes. Lastly, the Gent model predicts that instabilities in single layer tubes can be avoided under this boundary condition.

To conclude this section, we find that tubes subjected to traction free boundaries experience significantly larger expansions at lower voltages as a result of the freedom of the outer surface to deform. If the outer surface is fixed, thicker tubes are capable of larger expansions of the inner tube at the cost of higher voltages. It is also pointed out that by fixing the outer radius, instabilities can be avoided.

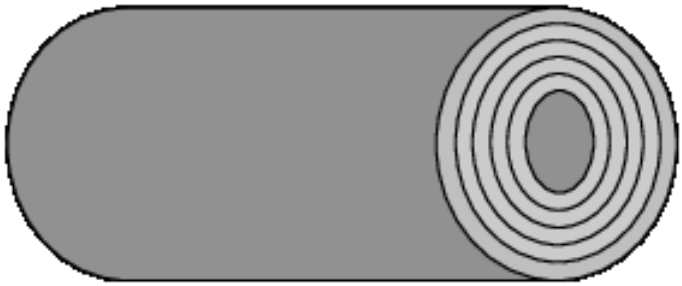

Figure 4: A schematic of a stacked cylindrical actuator.

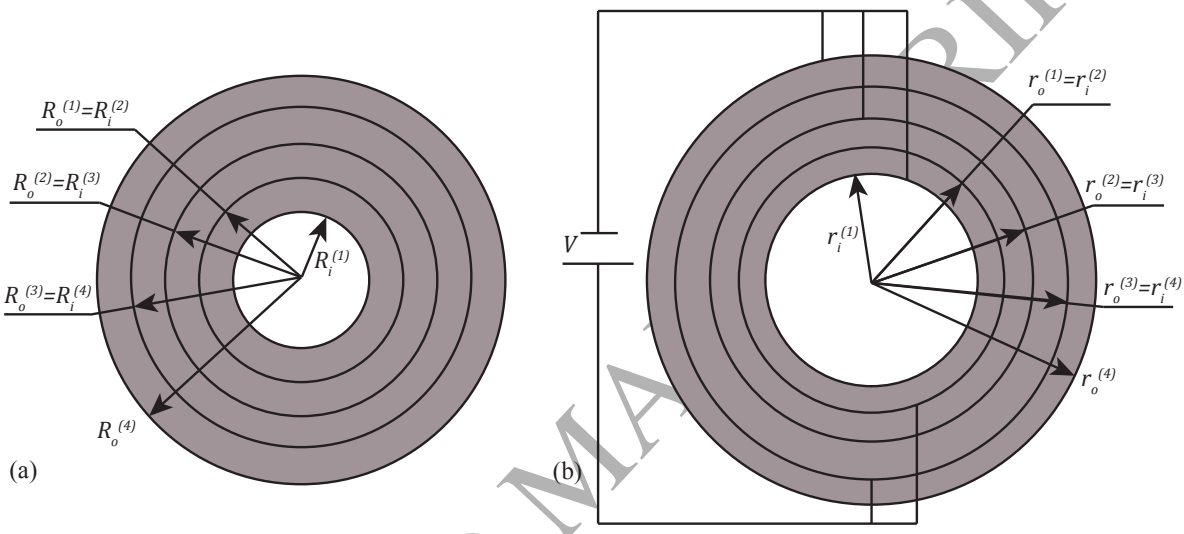

Figure 5: A cross section of a stacked cylindrical actuator (a) before and (b) after actuation.

4 The electro-mechanical response of a stacked multilayer tube

Consider next a tube composed of m stacked infinite cylindrical capacitors, where each capacitor is composed of a dielectric layer sandwiched between two flexible conductors (Fig. (4)). The capacitors are mechanically connected in series and electrically connected in parallel. The referential inner and outer radii of the i-th layer are denoted $R_i^{(i)}$ and $R_o^{(i)}$, respectively (Fig. (5a)). A potential difference V is applied across each layer and as a result the inner and outer radii at the current configuration are $r_i^{(i)}$ and $r_o^{(i)}$, respectively (Fig. (5b)). The electric field on the i-th layer is

$$\mathbf{E}^{(i)} = \frac{V}{\ln\left(\frac{r_o^{(i)}}{r_i^{(i)}}\right)} \frac{1}{r}\,\hat{\mathbf{r}}, \tag{34}$$

where $r_i^{(i)} \leq r \leq r_o^{(i)}$. From Eq. (34) one may deduce that the intensity of the electric field diminishes at layers that are further form the axis of the cylinder in a stacked cylindrical actuator

comprised of capacitors with an equal wall thickness.

The mapping of the material points from the reference to the current configuration of the i-th layer is

$$r = \sqrt{A^{(i)}\ \left(R^{(i)}\right)^2 + B^{(i)}}; \qquad \theta = \Theta; \qquad z = \frac{Z}{A^{(i)}}, \tag{35}$$

where $R_i^{(i)} \leq R \leq R_o^{(i)}$ and $A^{(i)}$ and $B^{(i)}$ are deformation related constants determined from the boundary conditions of the layer. Consequently, the deformation gradient of the i-th layer is given in Eq. (23) where A and B are replaced with $A^{(i)}$ and $B^{(i)}$, respectively.

The continuity constraint across the interface between the i-th and the $(i+1)$-th layers requires that

$$r_o^{(i)} = r_i^{(i+1)};\ \theta^{(i)} = \theta^{(i+1)};\ z^{(i)} = z^{(i+1)}. \tag{36}$$

From Eq. (36) we find that $A^{(i)} = A^{(i+1)} = A$ and $B^{(i)} = B^{(i+1)} = B$. In other words, the constants in the mappings of all layers are identical. Physically, this indicates that all layers are equally elongated along the longitudinal direction of the tube.

Furthermore, in order to maintain equilibrium

$$\sigma_{rr}^{(i)}\left(r = r_o^{(i)}\right) = \sigma_{rr}^{(i+1)}\left(r = r_i^{(i+1)}\right), \tag{37}$$

$$\sigma_{r\theta}^{(i)}\left(r = r_o^{(i)}\right) = \sigma_{r\theta}^{(i+1)}\left(r = r_i^{(i+1)}\right), \tag{38}$$

$$\sigma_{rz}^{(i)}\left(r = r_o^{(i)}\right) = \sigma_{rz}^{(i+1)}\left(r = r_i^{(i+1)}\right). \tag{39}$$

It can easily be shown that Eqs. (38) and (39) are automatically satisfied. Eq. (37) is satisfied through the integration constant that arises in the pressure term. Recall that this term stems from the incompressibility of the tube and is determined through the equilibrium equation in the radial direction. The pressure term for the i-th layer is given in Eqs. (27) and (29) for the neo-Hookean and the Gent models, respectively, where the integration constant C is replaced with $C^{(i)}$. Consequently, Eq. (37) contains four unknowns - A, B, $C^{(i)}$ and $C^{(i+1)}$. Note that in total there are $m-1$ such equations.

The tube is free to expand along the axial direction and therefore,

$$\int_{r_i^{(1)}}^{r_o^{(m)}} \int_0^{2\pi} \sigma_{zz}\, r\, \mathrm{d}r\, \mathrm{d}\theta = \sum_{i=1}^{m} \left[\int_{r_i^{(i)}}^{r_o^{(i)}} \int_0^{2\pi} \sigma_{zz}^{(i)}\, r\, \mathrm{d}r\, \mathrm{d}\theta \right] = 0, \tag{40}$$

where the integration is carried from the inner radius of the innermost layer $r_i^{(1)}$ to the outer radius of the outermost layer $r_i^{(m)}$. Eq. (40) contains $m+2$ unknowns - A, B, and m unknowns that pertain to the integration constants $C^{(i)},\ i = 1, 2, ..., m$.

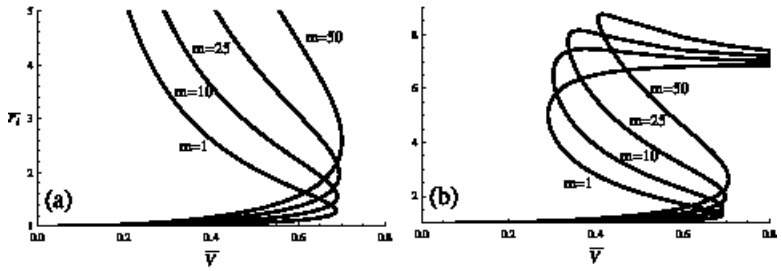

Figure 6: The relative inner radius $\overline{r_i}$ as a function of the normalized applied voltage $\overline{V}$ under traction free boundary conditions according to the (a) neo-Hookean and the (b) Gent models. The number of stacked layers m is denoted in the plots.

The boundary conditions on the inner and outer surfaces of the tube provide the two remaining equations that allow to determine the mapping parameters and the pressure terms in all of the layers. In total, we have a set of $m+2$ equations with $m+2$ unknowns.

Following the previous section, two boundary conditions are considered:

1. *Traction free tube* - the inner and outer surfaces of the tube are traction free. Accordingly, Eq. (32) can be rewritten as

$$\sigma_{rr}\left(r=r_i^{(1)}\right)=0; \qquad \sigma_{rr}\left(r=r_o^{(m)}\right)=0. \tag{41}$$

2. *Fixed outer radius* - the outer surface of the tube is fixed while the inner surface is free to deform. Accordingly, Eq. (33) is modified to

$$\sigma_{rr}\left(r=r_i^{(1)}\right)=0; \qquad r_o^{(m)}=R_o^{(m)}. \tag{42}$$

In the following, four cylindrical stacked actuators with $m=1$, $m=10$, $m=25$ and $m=50$ layers are examined under the two boundary conditions. The initial wall thickness of each layer is $H=0.1$ [mm] and the relative wall thickness $\overline{h}=\frac{r_o^{(m)}-r_i^{(1)}}{m\,H}$ is defined as the ratio between the sum of the wall thicknesses of all layers before and after the actuation. We recall the definitions $\overline{V}=\frac{V}{H}\sqrt{\frac{\varepsilon_r\varepsilon_0}{\mu}}$ and $\overline{r_i}=\frac{r_i}{R_i}$. As in the previous section, the layers assume the properties of VHB 4910 ($\mu=73$ [kPa], $\varepsilon_r=4.7$ and $J_m=89$).

Figs. (6a) and (6b) plot the relative inner radius as a function of the normalized applied voltage $\overline{V}$ for cylindrical stacked actuators with various layers according to the neo-Hookean (Eq. (19)) and the Gent (Eq. (21)) models, respectively. It is demonstrated that a given voltage induces larger expansions of the inner tube as the number of layers increases. Furthermore, we find that a larger inner radius is obtained at the point of instability as additional layers are mounted on the cylindrical actuator. Specifically, the values $\overline{r_i}=1.29$, $\overline{r_i}=1.56$, $\overline{r_i}=1.97$

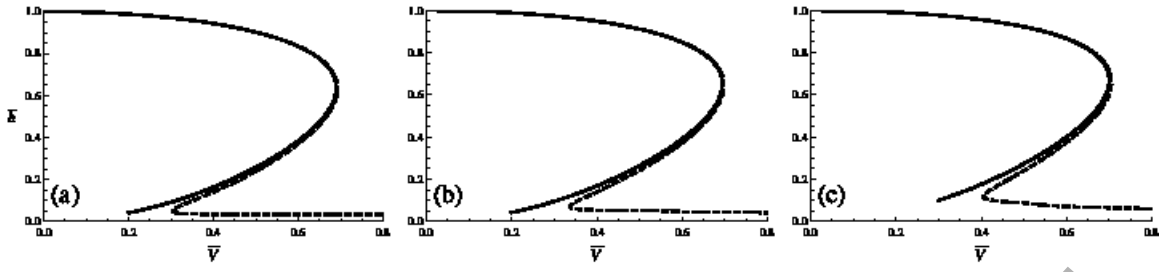

Figure 7: The relative wall thickness $\overline{h}$ as a function of the normalized applied voltage $\overline{V}$ under traction free boundary conditions for a stacked cylindrical actuator with (a) $m = 10$, (b) $m = 25$ and (c) $m = 50$. The continuous and the dashed curves correspond to the neo-Hookean (Eq. (19)) and the Gent (Eq. (21)) models, respectively.

and $\overline{r_i} = 2.59$ are obtained at a voltage $\overline{V} \approx 0.7$ for tubes with $m = 1$, $m = 10$, $m = 25$ and $m = 50$ layers, respectively. The range of possible inner radii improves as additional layers are stacked, and accordingly the performance of the actuator can be enhanced. Examination of the predicted inner radius according to the Gent model after the snap-through instability point (Fig. (6b)) reveals that larger inner radii can be achieved in cylindrical actuators with more layers.

Figs. (7a), (7b) and (7c) depict the relative wall thickness $\overline{h}$ as a function of $\overline{V}$ for cylindrical actuators composed of $m = 10$, $m = 25$ and $m = 50$ layers, respectively. Note that Fig. (2d) is the corresponding plot for $m = 1$. As before, the continuous and the dashed curves correspond to the neo-Hookean and the Gent models, respectively. The relative wall thickness is similar for the four examined stacked tubes. However, recall that the real wall thickness $h = m\,H\,\overline{h}$ and therefore, while the values of $\overline{h}$ are roughly equal, the actual wall thicknesses vary significantly. For example, the wall thickness of a stacked cylindrical tube with $m = 50$ layers is approximately five times that of a similar tube with $m = 10$ layers. From a practical viewpoint, while the addition of EAP layers conduces to the range of actuation radii, the expansion of the outer radius poses a design constraint that should be taken into account.

The response of a stacked cylindrical actuator with a fixed outer radius is studied next. Following Figs. (3a) and (3d) for a single-layer thin tube, Figs. (8a-c) and (8d-f) depict the predicted relative inner radius and the relative wall thickness as a function of the normalized applied voltage, respectively, for a stacked cylindrical actuator composed of $m = 10$, $m = 25$ and $m = 50$ layers. As before, the continuous and the dashed curves correspond to the neo-Hookean and the Gent models, respectively. Note that the $\overline{r_i}$ scales in Figs. (8a-c) are different. As expected, the feasible range of actuated radii increases as additional layers are mounted on the tube. It is again found that beyond a critical voltage no solutions exist according to the neo-Hookean model. Interestingly, while the response predicted by the Gent model of stacked cylindrical actuators with $m = 1$ and $m = 10$ layers is stable, Figs. (8b) and (8c) show that the addition of layers may induce an unstable behavior. Specifically, a snap through from $\overline{r_i} \approx 2$ to $\overline{r_i} \approx 3.2$ at a voltage $\overline{V}_c \approx 0.71$ is predicted in a stacked cylindrical actuator with $m = 25$. This

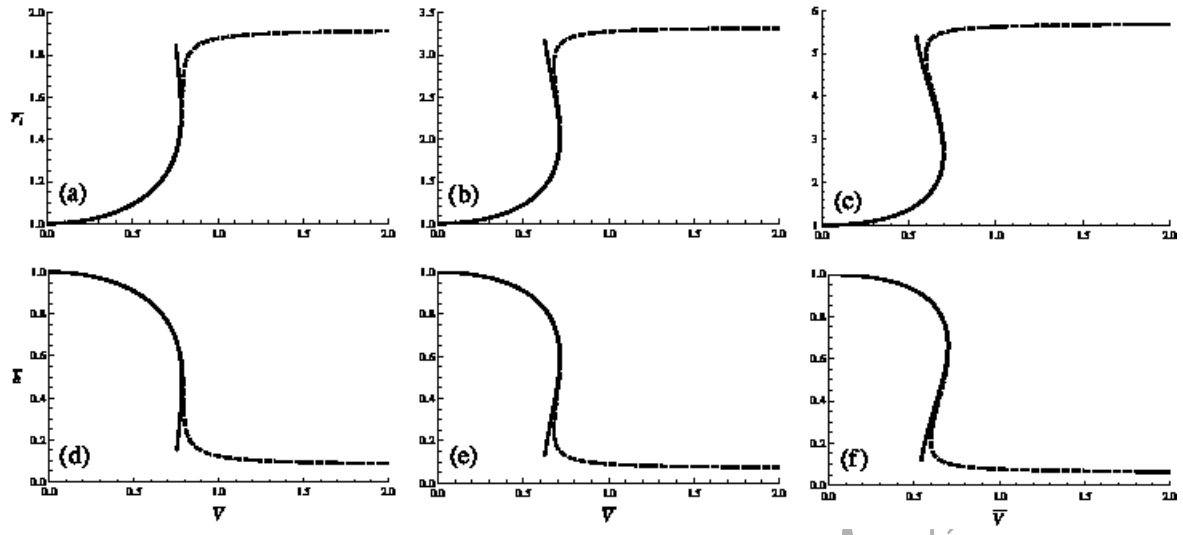

Figure 8: The relative inner radius $\overline{r_i}$ (a-c) and the relative wall thickness $\overline{h}$ (d-f) as a function of the normalized applied voltage $\overline{V}$ subjected to a fixed outer radius. The continuous and the dashed curves correspond to the neo-Hookean (Eq. (19)) and the Gent (Eq. (21)) models, respectively. Figs. (a,d), (b,e) and (c,f) correspond to a cylindrical actuator with $m = 10$, $m = 25$ and $m = 50$, respectively.

effect becomes more pronounced as the number of layers increases. Practically, the instability stems from the continuity constraints and the electrical and the mechanical forces due to the induced non-homogenous electric field. Note that the electric field acting on the outer layers is weaker and, as a consequence, the reduction in wall thickness of these layers is smaller. However, the continuity constraint along the axis of the cylinder enforces a constant elongation of all layers which, in turn, intensifies the pressure term of the inner layers in order to satisfy Eq. (40). This may result in a snap-through instability which is amplified as additional layers are mounted on the stacked cylindrical actuator.

To conclude, we find that a wider range of inner radii is available in stacked cylindrical actuators with more layers. Nevertheless, the enhanced performance comes at a cost. Subjected to traction free boundary conditions, the expansion of the outer surface of a stacked cylindrical actuator is commensurate with the number of layers. This effect may pose design constraints and cannot be dismissed. Under a fixed outer radius, adding layers to the actuator may lead to instabilities. It is again emphasized that in order to attain a relative inner radius $\overline{r_i}$, lower voltages are required in the traction free tube.

5 Concluding remarks

This work examines the capabilities of a stacked cylindrical actuator with the applicative aim of electrically controlling the inner radius. From a practical point of view, such a device can be

used in a variety of applications requiring soft tubes with flexible openings.

This work begins with the examination of the electromechanical response of three single-layer tubes with the same inner radius and different wall thicknesses under two boundary conditions - traction free boundaries and a fixed outer radius. It is found that, subjected to traction free boundaries, the inner and the outer radii increase. Additionally, it is demonstrated the range of available actuation radii increases with the thickness of the layer, as one might expect. Furthermore, the well-established models employed in this paper predict an instability in a traction free tube. This effect can be avoided by fixing the outer radius. It is highlighted that in a single layer tube a compressive stress is required in order to do so.

Next, the electromechanical response of a stacked cylinder actuator is studied. This actuator is comprised of polymer tubes with equal initial wall thicknesses that are mechanically connected in series and electrically connected in parallel. This configuration provides the ability to induce high electric fields across each layer and overcomes the main limitation of EAPs. Mechanically, the accumulated displacement of the stacked layers allows to attain a wider range of available inner radii and, practically, enhances the capabilities of the actuator.

Two boundary conditions are again considered. Subjected to traction free boundaries, increasing the number of layers in the cylindrical actuator enables a wider range of applicative inner radii. Interestingly, the critical voltage that induces instability is independent of the number of layers within the discussed range. When the outer surface is fixed, it is shown that a wider range of applicative inner radii is available in tubes comprised of more layers. Surprisingly, the study reveals that while instabilities can be avoided in stacked cylindrical actuators with a few layers, this effect may arise in actuators comprised of many cylindrical films.

This study discusses the feasibility of EAPs in a stacked cylindrical setting and examines the possible limitations of design that may arise in its implementation.

Acknowledgments The author would like to thank Gal deBotton for helpful discussions.

References

Y. Bar-Cohen. EAP history, current status, and infrastructure. In Y. Bar-Cohen, editor, *Electroactive Polymer (EAP) Actuators as Artificial Muscles*, chapter 1, pages 3–44. SPIE press, Bellingham, WA, 2001.

M. Bozlar, C. Punckt, S. Korkut, J. Zhu, C. C. Foo, Z. Suo, and I. A. Aksay. Dielectric elastomer actuators with elastomeric electrodes. *Applied Physics Letters*, 101(9):091907, 2012.

F. Carpi and D. De Rossi. Dielectric elastomer cylindrical actuators: electromechanical mod-

elling and experimental evaluation. *Materials Science and Engineering: C*, 24(4):555–562, 2004.

F. Carpi, A. Migliore, G. Serra, and D. De Rossi. Helical dielectric elastomer actuators. *Smart Materials and Structures*, 14(6):1210, 2005.

F. Carpi, C. Salaris, and D. De Rossi. Folded dielectric elastomer actuators. *Smart Materials and Structures*, 16(2):S300, 2007.

N. Cohen. Enhancing the electro-mechanical response of stacked dielectric actuators. *Submitted for publication*, 2016.

N. Cohen and G. deBotton. Multiscale analysis of the electromechanical coupling in dielectric elastomers. *European Journal of Mechanics - A/Solids*, 48(0):48 – 59, 2014.

N. Cohen, A. Menzel, and G. deBotton. Towards a physics-based multiscale modelling of the electro-mechanical coupling in electro-active polymers. *Proceedings of the Royal Society of London A: Mathematical, Physical and Engineering Sciences*, 472(2186), 2016. doi: 10.1098/rspa.2015.0462.

A. Dorfmann and R. W. Ogden. Nonlinear electroelasticity. *Acta Mechanica*, 174:167–183, 2005.

J. Due, S. Munk-Nielsen, and R.O. Nielsen. Energy harvesting with di-electro active polymers. In *Power Electronics, Machines and Drives (PEMD 2010), 5th IET International Conference on*, pages 1–6. IET, 2010.

A. N. Gent. A new constitutive relation for rubber. *Rubber Chemistry and Technology*, 69: 59–61, 1996.

G. Kovacs and L. Düring. Contractive tension force stack actuator based on soft dielectric eap. In *SPIE Smart Structures and Materials+ Nondestructive Evaluation and Health Monitoring*, pages 72870A–72870A. International Society for Optics and Photonics, 2009.

G. Kovacs, P. Lochmatter, and M. Wissler. An arm wrestling robot driven by dielectric elastomer actuators. *Smart Materials and Structures*, 16(2):S306, 2007.

G. Kovacs, L. Düring, S. Michel, and G. Terrasi. Stacked dielectric elastomer actuator for tensile force transmission. *Sensors and Actuators A: Physical*, 155(2):299–307, 2009.

P. Lotz, M. Matysek, and H. F. Schlaak. Fabrication and application of miniaturized dielectric elastomer stack actuators. *Mechatronics, IEEE/ASME Transactions on*, 16(1):58–66, 2011.

T. McKay, B. O'Brien, E. Calius, and L. Anderson. An integrated, self-priming dielectric elastomer generator. *Applied Physics Letters*, 97:062911, 2010.

R. M. McMeeking, C. M. Landis, and S. M. A. Jimenez. A principle of virtual work for combined electrostatic and mechanical loading of materials. *International Journal of Nonlinear Mechanics*, 42(6):831–838, 2007.

M. Moscardo, X. Zhao, Z. Suo, and Y. Lapusta. On designing dielectric elastomer actuators. *Journal of Applied Physics*, 104(9):093503, 2008.

Q. Pei, R. Pelrine, S. Stanford, R. Kornbluh, and M. Rosenthal. Electroelastomer rolls and their application for biomimetic walking robots. *Synthetic Metals*, 135:129–131, 2003.

S. Rudykh, K. Bhattacharya, and G. deBotton. Snap-through actuation of thick-wall electroactive balloons. *International Journal of Non-linear Mechanics*, 47:206–209, 2012.

H. F. Schlaak, M. Jungmann, M. Matysek, and P. Lotz. Novel multilayer electrostatic solid state actuators with elastic dielectric. In *Smart Structures and Materials*, pages 121–133. International Society for Optics and Photonics, 2005.

G. Shmuel. Manipulating torsional motions of soft dielectric tubes. *Journal of Applied Physics*, 117(17):174902, 2015.

G. Shmuel and G. deBotton. Axisymmetric wave propagation in finitely deformed dielectric elastomer tubes. *Proceedings of the Royal Society of London A: Mathematical, Physical and Engineering Sciences*, 469(2155), 2013. ISSN 1364-5021. doi: 10.1098/rspa.2013.0071.

M. Singh and A.C. Pipkin. Controllable states of elastic dielectrics. *Archive for Rational Mechanics and Analysis*, 21(3):169–210, 1966.

R. Springhetti, E. Bortot, G. deBotton, and M. Gei. Optimal energy-harvesting cycles for load-driven dielectric generators in plane strain. *IMA Journal of Applied Mathematics*, 79(5): 929–946, 2014. doi: 10.1093/imamat/hxu025.

Z. Suo, X. Zhao, and W.H. Greene. A nonlinear field theory of deformable dielectrics. *Journal of the Mechanics and Physics of Solids*, 56(2):467–486, 2008.

A. Tutcuoglu and C. Majidi. Energy harvesting with stacked dielectric elastomer transducers: Nonlinear theory, optimization, and linearized scaling law. *Applied Physics Letters*, 105(24): 241905, 2014. doi: http://dx.doi.org/10.1063/1.4904473. URL `http://scitation.aip.org/content/aip/journal/apl/105/24/10.1063/1.4904473`.